Energy & Environmental Science

COMMUNICATION

View Article Online
View Journal | View Issue

Cite this: *Energy Environ. Sci.*, 2017, **10**, 528

Received 11th December 2016,
Accepted 5th January 2017

DOI: 10.1039/c6ee03597c

www.rsc.org/ees

The structural origin of enhanced piezoelectric performance and stability in lead free ceramics†

Ting Zheng,‡[a] Haijun Wu,‡[b] Yuan Yuan,‡[a] Xiang Lv,[a] Qi Li,[c] Tianlu Men,[c] Chunlin Zhao,[a] Dingquan Xiao,[a] Jiagang Wu,*[a] Ke Wang,*[c] Jing-Feng Li,[c] Yueliang Gu,[d] Jianguo Zhu[a] and Stephen J. Pennycook*[b]

Lead-based piezoelectric materials are currently facing global restrictions due to their lead toxicity. Thus it is urgent to develop lead-free substitutes with high piezoelectricity and temperature stability, among which, potassium-sodium niobate [(K,Na)NbO_3, KNN] has the most potential. It is very difficult to simultaneously achieve high piezoelectric performance and reliable stability in KNN-based systems. In particular, the structural/physical origin for their high piezoelectricity is still unclear, which hinders property optimization. Here we report the achievement of high temperature stability (less than 10% variation for electric field-induced strain from 27 °C to 80 °C), good fatigue properties (stable up to 10^6 cycles) as well as an enhanced piezoelectric coefficient (d_{33}) of 525 pC N^{-1} in $(1-x)(K_{1-y}Na_y)(Nb_{1-z}Sb_z)O_3$–$xBi_{0.5}(Na_{1-w}K_w)_{0.5}HfO_3$ (KNNS–BNKH) ceramics through manipulating the rhombohedral–tetragonal (R–T) phase boundary. The structural origin of their high piezoelectric performance can be attributed to a hierarchical nanodomain architecture, where the local structure inside nanodomains comprises R and T nanotwins. The physical origin can be attributed to low domain wall energy and nearly vanishing polarization anisotropy, facilitating easy polarization rotation among different states. We believe that the new breakthrough will open a window for the practical applications of KNN-based ceramics.

Broader context

Environmental protection and concern for human health is the urgent driving force for eliminating lead from current commercial piezoelectric materials. However, for lead-free piezoelectric materials, achieving a high piezoelectric coefficient and simultaneously good stability over the required operating range has proved to be elusive. In particular, it is well known that the excellent properties of both the lead-based and lead-free compounds can be obtained at phase boundaries. However, the structural/physical origin for high piezoelectricity is still not very clear, which has been the longstanding obstacle to designing new lead-free materials with improved properties. Here we achieved excellent comprehensive performance: a giant piezoelectric coefficient (d_{33} ~ 525 pC N^{-1}) in potassium-sodium niobate lead-free ceramics; good temperature stability (temperature variation less than 10% from 27 °C to 80 °C); and good fatigue properties (stable up to 10^6 cycles). Furthermore, we report PFM/TEM results revealing the key structural origin: the hierarchical nanodomain architecture comprising rhombohedral and tetragonal nanotwins. Such a structure facilitates easy polarization rotation between different states and leads to outstanding properties. We use just conventional solid-state synthesis and hence believe that our breakthrough in d_{33} and stability will open a new window for the practical applications of lead-free piezoceramics.

High performance piezoceramics with direct conversion between mechanical and electrical energy have been widely used in electronic devices such as actuators, sensors, transducers, and so on.[1–10] Lead zirconate titanate [Pb(Zr,Ti)O_3, PZT]-based ceramics have won much more attention due to their excellent piezoelectricity as well as high Curie temperature (T_C).[1] However, lead-based piezoceramics will be prohibited in the future with increasing attention to environmental problems and human health. Therefore, developing lead-free piezoceramics as replacements for PZT has become one of the most urgent tasks. In recent years, there have been numerous investigations of lead-free materials, such as $BaTiO_3$ (BT),[2] $Bi_{0.5}Na_{0.5}TiO_3$ (BNT),[3] $BiFeO_3$ (BFO),[4] and (K,Na)NbO_3 (KNN)-based ceramics.[5,6] However, some shortcomings hindered their continuous developments, such as low Curie temperature for BT-based ceramics, poor piezoelectricity for BNT-based ceramics, and high leakage current for BFO-based ceramics. KNN-based ceramics have therefore become the most likely materials to replace Pb-based materials due to their large piezoelectricity and high Curie temperature.[6]

In order to improve the piezoelectric activity of KNN-based ceramics, much attention has been given to the construction of

[a] *Department of Materials Science, Sichuan University, 610064, Chengdu, P. R. China. E-mail: wujiagang0208@163.com, msewujg@scu.edu.cn*
[b] *Department of Materials Science and Engineering, National University of Singapore, 117575, Singapore. E-mail: steve.pennycook@nus.edu.sg*
[c] *State Key Laboratory of New Ceramics and Fine Processing, School of Materials Science and Engineering, Tsinghua University, 100084, Beijing, P. R. China. E-mail: wang-ke@tsinghua.edu.cn*
[d] *Shanghai Synchrotron Radiation Facility, Shanghai Institute of Applied Physics, Chinese Academy of Sciences, Pudong New Area, Shanghai 201204, P. R. China*
† Electronic supplementary information (ESI) available. See DOI: 10.1039/c6ee03597c
‡ Equal contribution.

phase boundaries driven by composition modifications.[5–7,11–15] The construction of orthorhombic–tetragonal (O–T) phase boundaries has been widely used to promote d_{33} of KNN-based ceramics, but d_{33} is normally limited to 200–300 pC N^{-1},[6,7,13] insufficient for replacing PZT. For further promoting their piezoelectric activity, we constructed a new phase boundary (rhombohedral–tetragonal, R–T) and achieved improved piezoelectricity (d_{33} = 425–570 pC N^{-1}).[14–18] However, the structural/physical origin for high piezoelectricity is still not very clear, which has been the longstanding obstacle to designing new lead-free materials with improved properties.

Both excellent piezoelectricity and reliable temperature/field-cycling stability are required for practical applications.[19–23] Previously, it was reported that PZT-based ceramics possess a good temperature stability of d_{33} due to the intrinsic characteristics of morphotropic phase boundaries (MPB). However, the KNN-based ceramics have polymorphic phase boundaries (PPB) instead of MPB, leading to a strong temperature sensitivity of the piezoelectric response.[5–7] For example, in $0.948KNN–0.052LiSbO_3$ ceramics, the inverse piezoelectric coefficient (d_{33}*) can decrease from 355 pm V^{-1} at room temperature to 250 pm V^{-1} at 50 °C (30% variation).[19] In order to solve this problem, $CaTiO_3$ was added to improve the temperature stability by shifting the corresponding $T_{O–T}$ below room temperature,[20] but unfortunately their d_{33} was seriously deteriorated. Therefore, it is difficult to realize both a high piezoelectric response and good temperature stability in KNN-based ceramics.

In this work, we designed a new ceramic system of $(1-x)(K_{1-y}Na_y)(Nb_{1-z}Sb_z)O_3–xBi_{0.5}(Na_{1-w}K_w)_{0.5}HfO_3$ (KNNS–BNKH), where an R–T phase boundary can be constructed by optimizing x, y, z and w. We achieved a giant d_{33} ($\sim$525 pC N^{-1}) in the ceramics with x = 0.035, y = 0.52, z = 0.05 and w = 0.18. More importantly, improved temperature stability of d_{33}* (a reduction of less than 10% from 27 °C to 80 °C) and good fatigue behavior (stable up to 10^6 cycles) were also achieved. To reveal the structural/physical origin of high performance, the domain structure was probed *via* advanced microscopy techniques. Both low domain wall energy and nearly vanishing polarization anisotropy of the hierarchical phase-coexisting nanodomains are responsible for high piezoelectric performance, facilitating polarization rotation among different states and thus leading to superior properties.

1. Experimental section

Our KNNS–BNKH ceramics were fabricated by using the conventional solid-state methods. Raw materials are Na_2CO_3 (99.8%), K_2CO_3 (99%), Nb_2O_5 (99.5%), Sb_2O_3 (99.99%), Bi_2O_3 (99.999%) and HfO_2 (99%). All raw materials were ball milled for 24 h with alcohol, and then dried and calcined at 850 °C for 6 h. These calcined powders were mixed with a binder of 8 wt% polyvinyl alcohol (PVA) and pressed into pellets with a diameter of 10 mm and a thickness of 1 mm under a pressure of 10 MPa. All samples were sintered at 1060–1090 °C for 3 h in air and poled at 20 °C in a silicon oil bath under a direct current electric field of 1–3 kV mm^{-1}. The overall processing equipment, real green and sintered samples fabricated in this study are presented in Fig. S1 of the ESI.†

An HR LabRAM Raman spectroscopy system was used to measure the temperature (−100–210 °C) dependence of the Raman spectrum, where a 514 nm Ar laser was used for excitation. The piezoelectric constant d_{33} was measured using a quasi-static piezoelectric constant testing meter (ZJ-3A, Institute of Acoustics, Chinese Academy of Sciences). The temperature dependences of field-dependent piezoelectric coefficient $d_{33}(E)$ hysteresis loops, unipolar and bipolar strain $S(E)$ curves, and polarization $P(E)$ hysteresis loops were investigated on a ferroelectric tester (aixACCT TF Analyzer 1000, Germany). Their $d_{33}(E)$ hysteresis loops were measured by applying a triangular signal of 2 kV mm^{-1} and f = 1 Hz, on which an AC voltage of 25 V at 250 Hz was superimposed. Unipolar strain hysteresis was measured using a unipolar triangular signal of 2 kV mm^{-1} at 1 Hz. A bipolar electric field of 2 kV mm^{-1} at 1 Hz was applied to obtain polarization $P(E)$ hysteresis loops and bipolar strain $S(E)$ curves. Unipolar fatigue behavior measurements were performed using the aixACCT TF Analyzer 1000 (aixACCT Systems GmbH, Germany). Piezoelectric force microscopy (PFM) measurements were carried out using a commercial microscope (MFP-3D, Asylum Research, Goleta, CA), applied to a conductive Pt–Ir coated cantilever PPP-NCHPt (Nanosensors, Switzerland). Vertical and lateral PFM images were taken to identify domain structures, which give information about the distribution of the out-of-plane and in-plane components of polarization, respectively. In this work, different PFM measurement modes have been applied to achieve our objectives. For example, the dual AC resonance tracking (DART) mode was applied to reflect the temperature stability of the domain structure, as shown in Fig. 3, while the vector mode with an electric field was applied to reflect the electric field stability of the domain structure, as shown in Fig. 4. Lastly, in order to obtain nanoscale lamellar domains, the vector mode without the applied electric field was used, as shown in Fig. 5. TEM sample preparation was performed by subsequent cutting, polishing, dimpling and ion milling. Transmission electron microscopy (TEM) and convergent-beam electron diffraction (CBED) were carried out using a JEM-2010F and JEM-3010 (JEOL) microscope. *In situ* synchrotron X-ray diffraction measurements were carried out at the Shanghai Synchrotron Radiation Facility with a beam line 14B1 (λ = 1.2348 Å).

2. Results and discussion

XRD patterns and temperature-dependent dielectric constant (ε_r–T) curves were used to identify the phase structures of the ceramics (see Fig. S2 and S3 of the ESI†). Fig. 1(a and b) show the phase diagrams of the ceramics as a function of x and z contents. One can find from Fig. 1(a) and (b) that T_C decreases linearly with the increase of x and z. In addition, their $T_{R–O}$ and $T_{O–T}$, respectively, increase and decrease as both x and z increase, resulting in the formation of an R–T phase boundary in the composition range of $0.035 \le x \le 0.05$ and $0.045 \le z \le 0.08$. In order to further identify the formation of the R–T phase

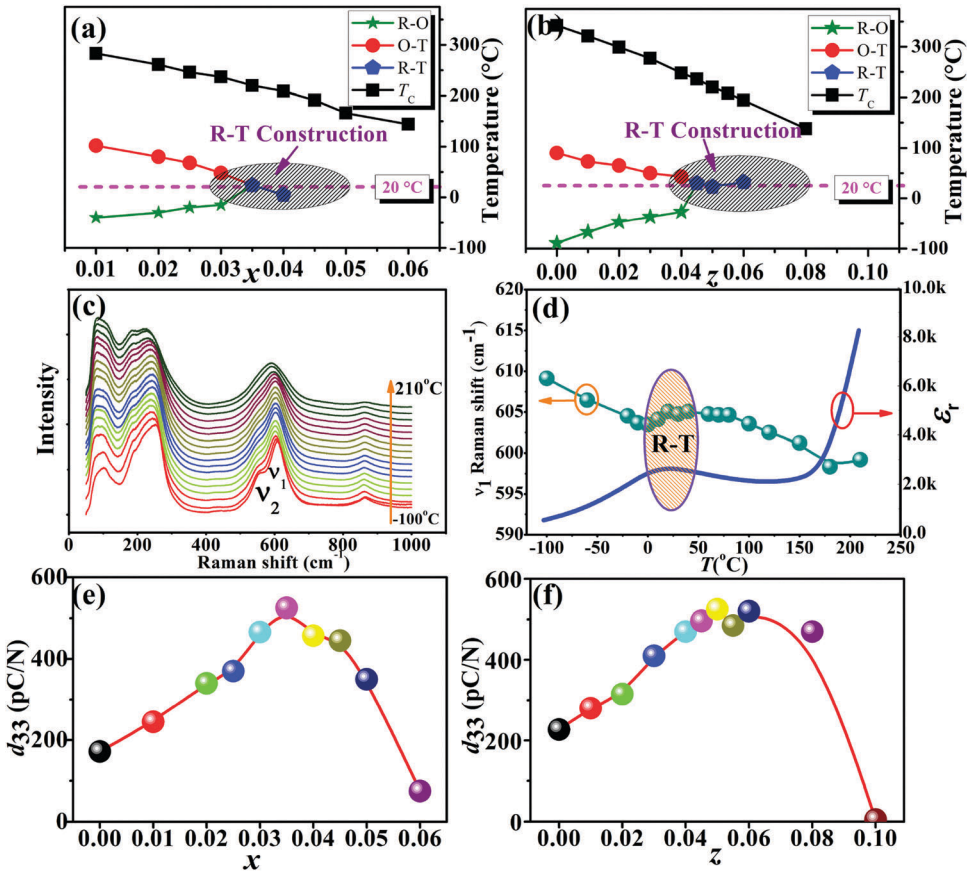

Fig. 1 (a and b) Phase diagrams of the ceramics as a function of x and z contents. (c) Evolution of Raman spectra with temperature for the ceramic with x = 0.035, y = 0.52, z = 0.05 and w = 0.18. (d) Evolution of the ν_1 mode and dielectric permittivity as a function of temperature ranging from −100 °C to 210 °C. (e and f) d_{33} of the ceramics as a function of x and z contents.

boundary, the temperature-dependent Raman spectra of the ceramics with x = 0.035, y = 0.52, z = 0.05 and w = 0.18 were measured, as shown in Fig. 1(c). In general, ν_1 (~600 cm^{-1}) and ν_2 (~550 cm^{-1}) vibrational modes are associated with BO_6 perovskite octahedra.[24,25] The ν_1 mode becomes broadened and its peak position shifts with increasing temperature, while the ν_2 mode gradually becomes weak. In accordance with literature studies,[24,25] we magnified and fitted Raman spectra in the wavenumber range of 500–700 cm^{-1} to detect the ν_1 peak position. The temperature-dependent ν_1 peak position and dielectric constant are simultaneously shown in Fig. 1(d). The wavenumber decreases linearly when the temperature increases from −100 to 0 °C. With further increasing temperatures, the wavenumber increases and then decreases, reaching the peak value for 20 °C. In this work, we confirmed that its T_{R-T} is about 20 °C according to the corresponding ε_r–T curve. As a result, the temperature dependence of both Raman spectra and the dielectric constant also strongly supports the existence of an R–T phase boundary at room temperature. Correspondingly, the piezoelectricity is closely related to the phase structure of the ceramics. As shown in Fig. 1(e) and (f), a giant d_{33} can be achieved in the ceramics by modifying their compositions. For example, a d_{33} of >400 pC N^{-1} can be achieved in a wide composition range of $0.03 \leq x \leq 0.05$ and $0.045 \leq z \leq 0.08$ with multiple phase boundaries. In particular, the largest d_{33} of ~525 pC N^{-1} can be achieved in the ceramics with x = 0.035, y = 0.52, z = 0.05, and w = 0.18 with the R–T phase boundary. The phase diagrams and the corresponding piezoelectric constants of the ceramics as a function of y and w are presented in Fig. S4 of the ESI.† The comprehensive performance (d_{33} = 525 pC N^{-1} and T_C = 220 °C) of this work is superior to the typical BT-based (high d_{33}, but too low T_C),[2] also to the newly reported BFO-based (high T_C, but low d_{33}),[26] and some PZT-based ceramics,[7] which could also compete with PZT-5H ceramics.[7] As is well known, the enhanced d_{33} is mainly due to the existence of the R–T phase boundary, leading to easy rotation of polarization.[14–18] The specific mechanisms for the enhanced piezoelectricity will be discussed later. Further composition dependence of ferroelectric and dielectric properties is presented in Fig. S5 and S6 of the ESI.†

The stability of electrical properties in lead-free piezoelectric materials is very important for industrial applications.[27] In the past, it was believed that KNN-based ceramics possess a poor temperature stability of d_{33} due to their PPBs, which are dependent on not only compositions but also temperatures.[5–7,19] We focused on the electric field dependence and temperature dependence of electrical properties in the ceramics with x = 0.035, y = 0.52, z = 0.05 and w = 0.18. Fig. 2(a) shows the electric field

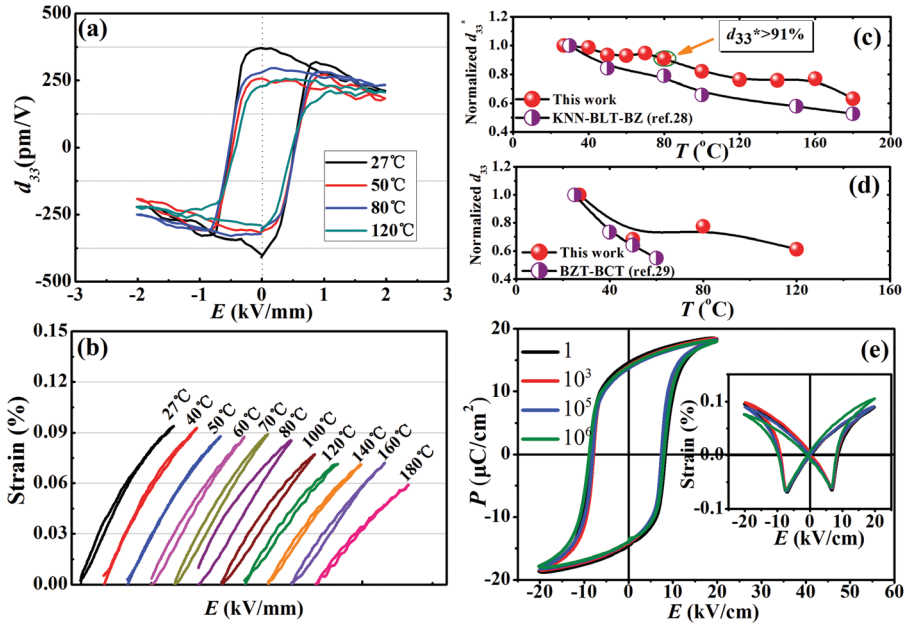

Fig. 2 Temperature-dependent (a) piezoelectric coefficient hysteresis loops; (b) unipolar piezoelectric strain; (c) normalized d_{33}* in this work and in KNN-BLT-BZ ceramics (ref. 28); (d) normalized d_{33} in this work and in BZT-BCT ceramics (ref. 29); and (e) unipolar fatigue P–E loops of the ceramics under f = 50 Hz, the inset in Fig. 2e is the unipolar fatigue S–E curves of the ceramics under f = 50 Hz.

dependence of $d_{33}(E)$ measured at various temperatures from 27 to 120 °C. The piezoelectric coefficient, also called small signal d_{33} (measured at low electric fields), is the positive value at the zero field in such $d_{33}(E)$ loops. Fig. 2(b) presents the unipolar piezoelectric strain $S(E)$ curves of the ceramics, measured from 27 to 180 °C at E = 2 kV mm^{-1}. The temperature dependences of normalized d_{33}* and d_{33} are shown in Fig. 2(c) and 3(d), respectively. The inverse piezoelectric coefficient, also called large signal d_{33}* (measured at high electric fields), calculated by S_{max}/E_{max}, varies less than 10% in the temperature range of 27–80 °C, indicating a relatively good temperature stability. Even if the measurement temperature reaches 160 °C, a high d_{33}* (~362 pm V^{-1}) is still maintained. In addition, a relatively good temperature stability of d_{33} was also observed, that is, d_{33} of the ceramics is about 77% for a measurement temperature of ~80 °C, as shown in Fig. 2(d). In order to compare the temperature stability between our work and others, the temperature stability of d_{33}* in $0.92K_{0.5}Na_{0.5}NbO_3$–$0.02Bi_{1/2}Li_{1/2}TiO_3$–$0.06BaZrO_3$ ceramics with an R–T phase boundary reported by Wang *et al.* and the temperature stability of d_{33} in $Ba(Zr_{0.2}Ti_{0.8})O_3$–$50(Ba_{0.7}Ca_{0.3})TiO_3$ ceramics reported by Ren *et al.* are included in Fig. 2(c) and (d).[28,29] It is clear that

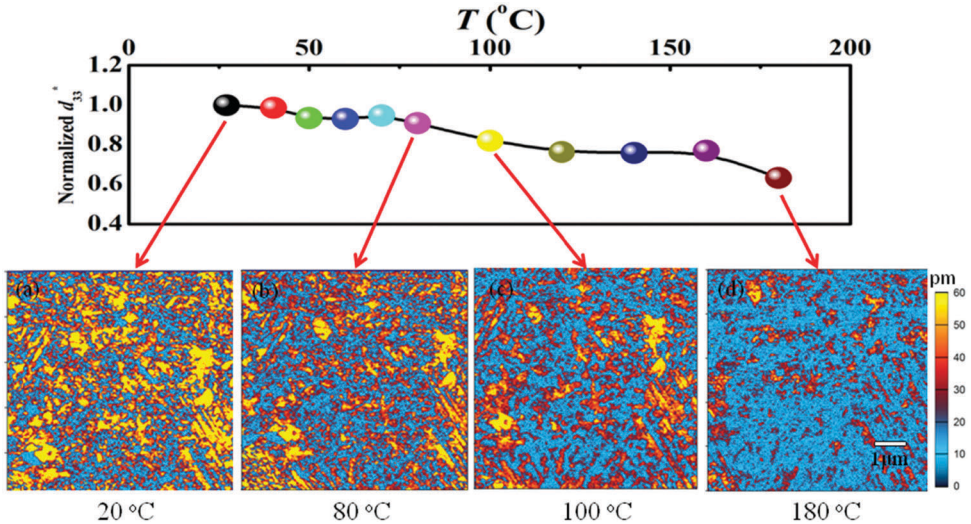

Fig. 3 Normalized d_{33}* and vertical piezoresponse force microscopy (VPFM) amplitude images of the ceramics with x = 0.035, y = 0.52, z = 0.05 and w = 0.18 at various temperatures.

an improved temperature stability of piezoelectricity has been achieved in this work. In addition, an improved temperature stability of ferroelectricity has also been achieved in the ceramics, as shown in Fig. S7 of the ESI.† For KNN-based materials, fatigue behavior is also very important for their practical applications.[21] The evolution of *P*–*E* loops and *S*–*E* curves under unipolar electric cycling of f = 50 Hz is displayed in Fig. 2(e). It can be seen that there are no obvious changes in *P*–*E* loops or *S*–*E* curves when unipolar electric cycling is within 10^6 cycles even if asymmetric behavior occurred in the *S*–*E* curves. Therefore, the improved fatigue stability can also be achieved in KNN-based ceramics.

Then we attempted to employ the *in situ* PFM technique in uncovering the underlying mechanism of the reliable temperature/field-cycling stability in the present system.[30,31] Fig. 3 shows the d_{33}* and vertical piezoresponse force microscopy (VPFM) images at various temperatures for the amplitude. It can be seen from Fig. 3(a) that a large number of nanoscale domains can be observed at ambient temperature, thus leading to the giant piezoelectricity. When the measurement temperature increases to 80 °C, a slight decrease in the number of nanodomains can be observed, as shown in Fig. 3(b). Furthermore, the amplitude of nanodomains gradually decreases with further increase of temperature, as shown in Fig. 3(c and d), thus leading to the linear decrease of d_{33}*. As a result, the high temperature stability (less than 10% variation for electric field-induced strain from ambient temperature to 80 °C) can be ascribed to the excellent stability of the nanodomains.

To reveal the improved electric-field stability of the present system, we investigated the effects of external electric fields on the relaxation time-dependent domain evolution, as indicated by PFM in Fig. 4. Fig. 4(a, c and e) show the VPFM images as a function of relaxation time; Fig. 4(b, d and f) correspond to the piezoresponse amplitude profiles generated from the line scan across the domains. It can be seen that the application of electric fields can induce the appearance of visible polarization stripes. The polarization stripes at 45 and 60 V are much brighter with respect to those at 30 and 15 V, indicating that the higher the voltage, the larger the amplitude or d_{33}, which can also be proved by the line scan profiles. In addition, the brightness of each stripe decreases with increase of relaxation time, demonstrating that relaxation occurs and the amplitude decreases. The amplitude *vs.* relaxation time with different voltages is displayed in Fig. S8 of the ESI.†

We now turn to the structural/physical origin of enhanced piezoelectricity. It was thought that the piezoelectric response consists of intrinsic (lattice) and extrinsic (domain wall movement) contributions.[32] For KNN-based ceramics, peak d_{33} occurs in the composition spanning phase boundaries.[14–18] The physical origin of the peak in d_{33} is interpreted as a flattening of the Gibbs free energy,[32] which is composition dependent, being largest near the MPB, facilitating polarization rotation and domain wall movement leading to an enhanced piezoelectric response. We might anticipate similar effects around the R–T phase boundary in our present ceramics. In addition,

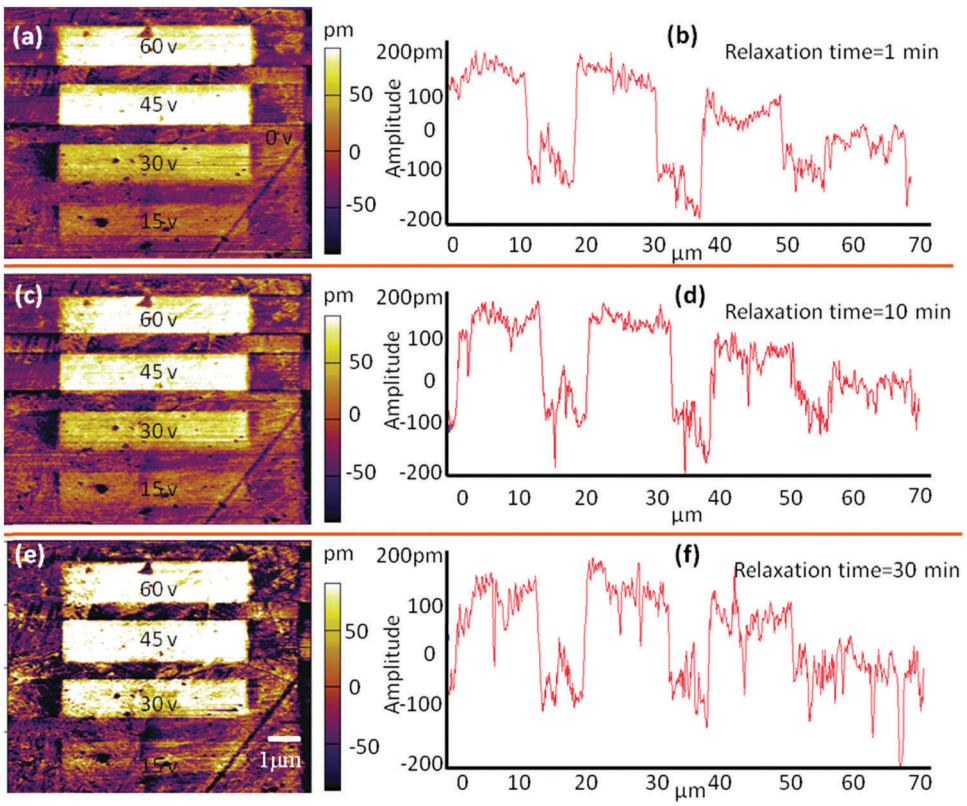

Fig. 4 (a, c and e) Piezoresponse mappings of the ceramics with x = 0.035, y = 0.52, z = 0.05 and w = 0.18 under various relaxation times; and (b, d and f) corresponding piezoresponse amplitude profiles generated from the line scan across the domains.

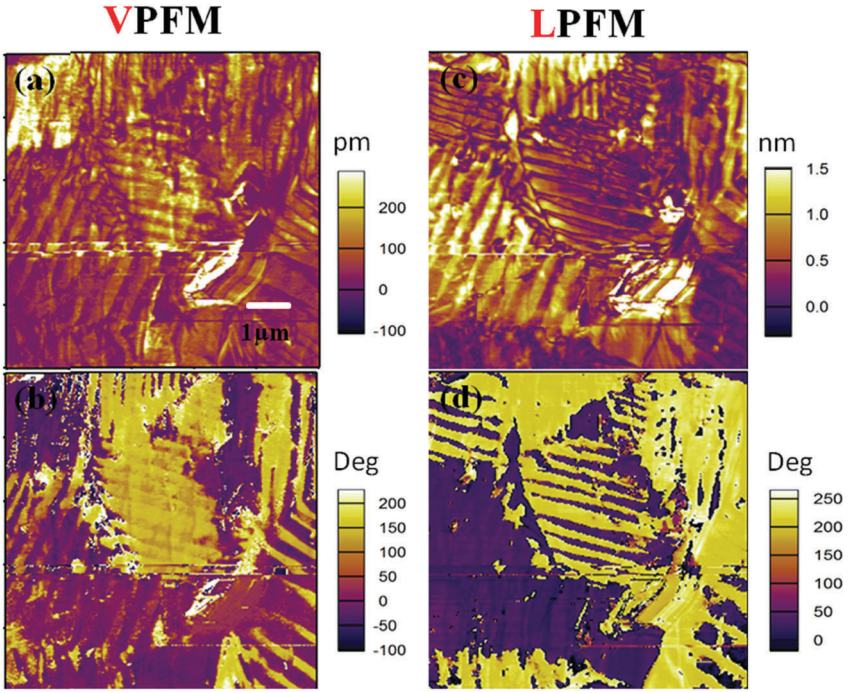

Fig. 5 Vertical piezoresponse force microscopy (VPFM) images for (a) amplitude and (b) phase of the ceramics with $x = 0.035$, $y = 0.52$, $z = 0.05$ and $w = 0.18$; and lateral piezoresponse force microscopy (LPFM) images for (c) amplitude and (d) phase of the same sample.

due to the close relationship between the domain structure and piezoelectricity,[33–35] we utilize PFM and transmission electron microscopy (TEM) to characterize the domain structure and further uncover the origin of the enhanced piezoelectricity. Fig. 5(a) and (b) display the VPFM images of the sample with $x = 0.035$, $y = 0.52$, $z = 0.05$ and $w = 0.18$ at ambient temperature for amplitude and phase, respectively. Fig. 5(c) and (d) respectively, show the lateral PFM (LPFM) images of the same sample for amplitude and phase. One can see that lamellar domains with widths of hundreds of nanometers and lengths of several micrometers dominate in the sample. According to the different orientations of polarization vectors, these lamellar domains may appear in either the out-of-plane component of polarization (VPFM images) or the in-plane component (LPFM images), while some may appear in both. Although the schematic of polarization variants has been determined in BFO thin films using angle-resolved piezoresponse force microscopy (AR-PFM), it is difficult to determine the polarization variants in KNN-based ceramics due to the complex polarization vector maps.[36] Previously, it was reported that such sub-micron domains play a critical role in promoting the piezoelectric performance of lead-based and lead-free piezoceramics.[33–35] The square root of domain wall energy is proportional to domain size,[37] and thus the sub-micron domains possess decreased domain wall energy and an improved flexibility compared with the micron domains in normal ferroelectric materials.[38]

To further reveal the underlying mechanisms of high piezoelectric performance, representative TEM bright-field images of ferroelectric domains are shown in Fig. 6 and Fig. S9 (ESI†). Compared with the classical microscale ferroelectric domains,[38] the domains shown here are sub-microns (50–200 nm) in width and oriented along ⟨100⟩ directions, which is well consistent with the lamellar domain pattern in the PFM images (see Fig. 5). In the present work, all planes and directions are indexed to pseudocubic axes. In order to observe the detailed features, the sample was tilted close to the two-beam condition with only [110] or [100] reflections excited. In this condition with strong diffraction contrast, slim nanodomains (10–30 nm in width and 100–300 nm in length) can be seen inside the sub-micron domains and they are parallel to each other along ⟨110⟩ directions, as shown in Fig. 6(a). Furthermore, enlarged images of the two traces of nanodomains along [110] and [1$\bar{1}$0] are shown in Fig. 6(b)–(d). The periodic variation in intensity is due to the slight orientation difference between different variants in the twinned structure.

To further verify the local coexisting crystal symmetries inside the hierarchical nanodomains, we employed convergent-beam electron diffraction (CBED). The CBED method, with a probe size of a few nanometers (0.5–2.4 nm), can detect symmetry information within each nanodomain, which is quite difficult *via* X-ray and neutron diffraction due to their limited spatial resolution.[39–43] KNN-based materials undergo three-step phase transitions: from paraelectric cubic (C, $Pm\bar{3}m$) phase to ferroelectric phases, tetragonal (T, $P4mm$), orthorhombic (O, $Amm2$) and rhombohedral (R, $R3c$), successively. The detailed symmetry elements of T, O and R phases are summarized in Table S1 of the ESI.† The distortions of these low-symmetry lattices can be thought of as elongations of their parent cubic unit cell along an edge ([001] for T), along a face diagonal ([110] for O), or along a body diagonal ([111] for R), the so called spontaneous

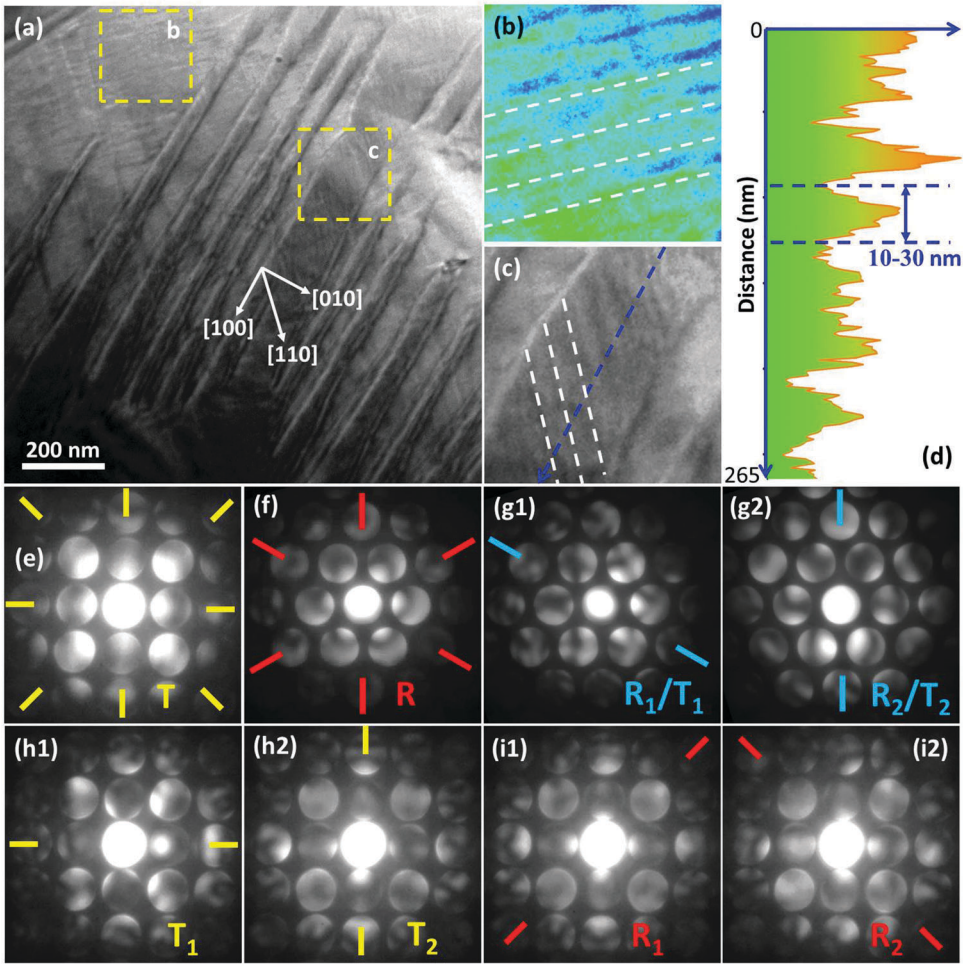

Fig. 6 Hierarchical nanodomain architecture and local symmetry inside nanodomains: (a) TEM bright-field image under the two-beam condition showing the hierarchical nanodomain structure, sub-micron domain along [100], with slim nanodomains along [110] and [1$\bar{1}$0]. (b) Enlarged and colored image showing slim nanodomains along [1$\bar{1}$0]. (c) Enlarged image showing slim nanodomains along [110]. (d) Line-scan intensity profile obtained from (c) showing intensity reflecting the periodical variation inside a sub-micron domain due to slim nanodomains. (e, h1, h2, i1 and i2) CBED patterns along the [001] zone axis. (f, g1 and g2) CBED patterns along the [111] zone axis. (e) CBED pattern showing 4mm symmetry. (f) CBED pattern showing 3m symmetry. (g1 and g2) CBED patterns obtained from adjacent nanodomains showing mirror planes along [11$\bar{2}$] and [1$\bar{2}$1]. The reflected structure symmetries are marked, where R/T means that either R or T is possible. (h1 and h2) CBED patterns obtained from adjacent nanodomains showing mirror planes along [100] and [010]. (i1 and i2) CBED patterns obtained from adjacent nanodomains showing mirror planes along [110] and [1$\bar{1}$0].

polarization (P_s) directions. These distortions introduce characteristic symmetry elements that can be identified *via* CBED; the tetragonal (T, *P*4*mm*) lattice possesses one 4-fold rotation axis along [001] and one mirror plane along [100]/[010]/[110]/[1$\bar{1}$0]; the orthorhombic (O, *Amm*2) lattice exhibits one mirror plane along [100]/[010] and a 2-fold rotation axis along [001]; the rhombohedral (R, *R*3*c*) lattice has one 3-fold rotation axis and one glide plane along [111]. Here we simulated CBED patterns of T and R phases and summarize the symmetries existing in [001], [110] and [111] pseudocubic zone axes with different polarization directions in Table S2 of the ESI.† The experimental CBED patterns obtained from [001], [110] and [111] are shown in Fig. 6(e)–(i2) and Fig. S10, S11 (ESI†) and identify the coexistence of R and T phases. The orthorhombic (O) phase is not observed in our case, as shown in Fig. S11 (ESI†), and thus the possibility of the orthorhombic (O) phase existing in the present composition at the R–T phase boundary can be excluded.

Furthermore, Fig. 6(h1, h2) and (i1, i2) show two sets of CBED patterns, which were obtained from adjacent nanodomains along [110] or [1$\bar{1}$0] as shown in Fig. 6(a)–(c). The CBED patterns shown in Fig. 6(h1, h2) exhibit mirror planes along [110] or [1$\bar{1}$0]; accordingly, the polarization direction in these adjacent nanodomains should be along [100] and [010], which is typical of (110)-type 90° tetragonal nanotwins. In contrast, Fig. 6(i1, i2) show CBED patterns with mirror planes along [110] and [1$\bar{1}$0], reflecting (110)-type 71° rhombohedral nanotwins with the twin variants along [111] and [1$\bar{1}$1]. Observing along the [111] zone axis, both tetragonal and rhombohedral twins exhibit similar mirror planes along one ⟨11$\bar{2}$⟩ direction [see Fig. 6(g1, g2)]. Thus the local symmetry inside the nanodomains of the present KNN system is

composed of (110)-type tetragonal (T) nanotwins and (110)-type rhombohedral (R) nanotwins.

The above domain structure has clearly formed the so-called hierarchical nanodomain architecture, which can be widely found in lead-based (PZT and PMN-PT) and lead-free (BZT-BCT) piezoelectric materials at the MPB composition.[38–43] Fig. 7(a)–(c) schematically show the crystallographic features of such hierarchical nanodomain architectures: nanodomains along ⟨110⟩ directions intersect at {100} domain walls, forming sub-micron domains along ⟨100⟩ directions; the nanodomains are actually the coexistence of {110}-type tetragonal and rhombohedral nanotwins. Derived from such nanoscaled structural coexistence, the physical origin of the high piezoelectric performance can be attributed to low domain wall energy and nearly vanishing polarization anisotropy, which facilitates easy polarization rotation between different states under an external field, as shown in Fig. 7(d). To illustrate it, we measured *in situ* synchrotron X-ray diffraction patterns on pseudocubic (100) and (220) reflections for the ceramics with $x = 0.035$, $y = 0.52$, $z = 0.05$ and $w = 0.18$ by applying external electric fields, as shown in Fig. 7(e) and (f). It can be clearly seen that both the intensity and position of the XRD patterns gradually changed after applying electric fields. To highlight the change in the peak intensity ratio, the ratio of low angle peak intensity to high angle peak intensity (I_1/I_2) for (100) and (220) reflections has been calculated and is plotted in Fig. 7(g). An obvious peak intensity ratio change can be observed and the change in the peak intensity ratio may be related to the rotation of the

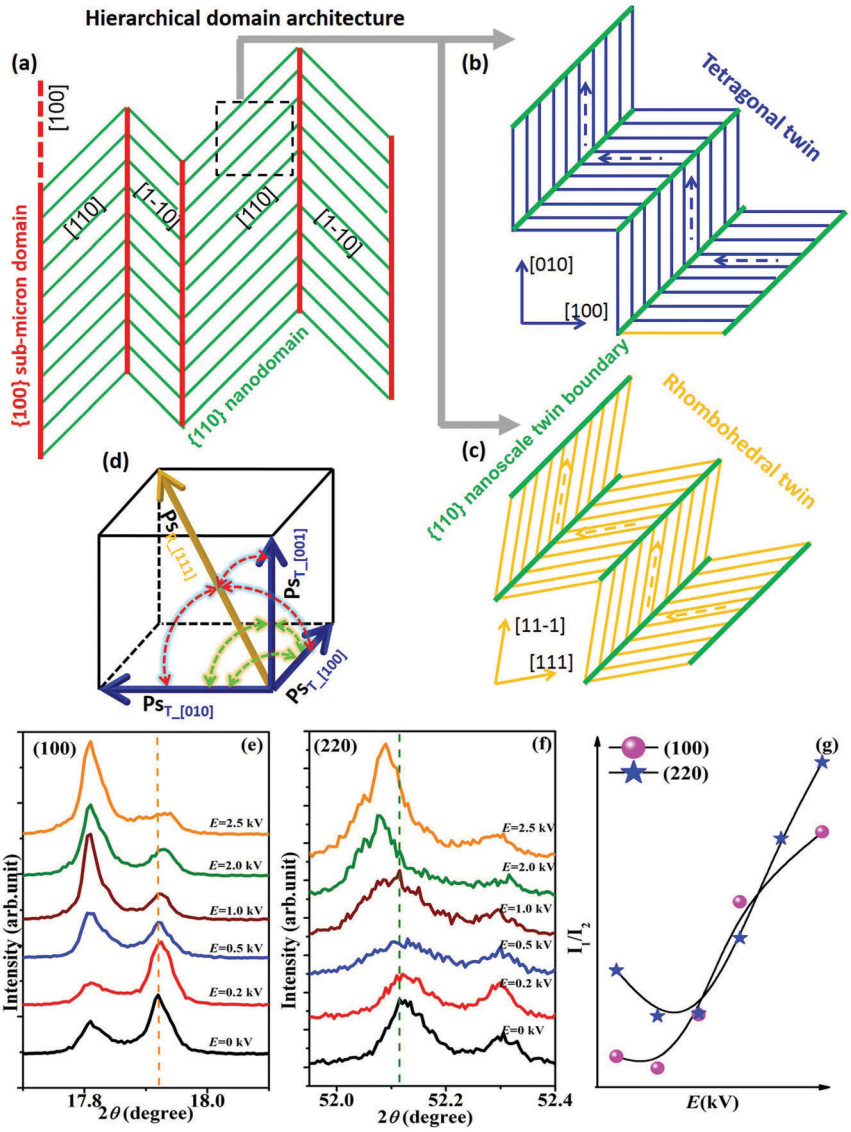

Fig. 7 Hierarchical nanodomain architecture and its change with the external electric field for the ceramic with $x = 0.035$, $y = 0.52$, $z = 0.05$ and $w = 0.18$: (a–c) schemes for the hierarchical nanodomain architecture, including sub-micron domains and nanodomains (tetragonal and rhombohedral nanotwins); (d) scheme for polarization direction rotation between R nanotwins and T nanotwins, the red and green dashed arrows indicate polarization rotation between different states; (e and f) evolution of the (100) and (220) pseudocubic reflections; (g) the ratio of low angle peak intensity to high angle intensity (I_1/I_2) for (100) and (220) pseudocubic reflections as a function of the electric field.

polarization direction between T and R states after electric poling,[38,44] while the shifts of peak positions are considered to be the results of the lattice distortion.[44]

3. Conclusions

In this communication, we realized both an enhanced d_{33} and its improved stability through a concrete example of $(1-x)(K_{1-y}Na_y)(Nb_{1-z}Sb_z)O_3$–$xBi_{0.5}(Na_{1-w}K_w)_{0.5}HfO_3$, and illuminated the structural/physical origin in detail. A high piezoelectric constant ($d_{33} \sim 525$ pC N^{-1}) was achieved at an R–T phase boundary by optimizing the composition, and then d_{33}* varies less than 10% in the temperature range of 27–80 °C and the fatigue behavior is stable up to 10^6 cycles. The origin is deduced to be easy polarization rotation within the hierarchical phase-coexisting nanodomains, which have low domain wall energy and nearly vanishing polarization anisotropy. We believe that this discovery will further stimulate the development of KNN-based ceramics with high d_{33} and reliable stability, which will benefit practical applications.

Acknowledgements

The authors gratefully acknowledge the support of the National Science Foundation of China (NSFC No. 51332003, 51102173, 51272164 and 51472169).

References

1 B. Jaffe, W. Cook and H. Jaffe, *Piezoelectric Ceramics*, Academic, New York, 1971, pp. 185–212.
2 W. F. Liu and X. B. Ren, *Phys. Rev. Lett.*, 2009, **103**, 257602.
3 T. Takenaka, K. O. Sakata and K. O. Toda, *Ferroelectrics*, 1990, **106**, 375–380.
4 T. Rojac, A. Bencan, B. Malic, G. Tutuncu, J. L. Jones, J. E. Daniels and D. Damjanovic, *J. Am. Ceram. Soc.*, 2014, **97**(7), 1993–2011.
5 Y. Saito, H. Takao, T. Tani, T. Nonoyama, K. Takatori, T. Homma, T. Nagaya and M. Nakamura, *Nature*, 2004, **432**, 84–87.
6 J. G. Wu, D. Q. Xiao and J. G. Zhu, *Chem. Rev.*, 2015, **115**(7), 2559–2595.
7 T. R. Shrout and S. J. Zhang, *J. Electroceram.*, 2007, **19**, 111.
8 C. K. Jeong, K. I. Park, J. Ryu, G. T. Hwang and K. J. Lee, *Adv. Funct. Mater.*, 2014, **24**(18), 2620–2629.
9 C. K. Jeong, K. I. Park, J. K. Son, G. T. Hwang, S. H. Lee, D. Y. Park, H. E. Lee, H. K. Lee, M. Byun and K. J. Lee, *Energy Environ. Sci.*, 2014, **7**, 4035–4043.
10 K. I. Park, S. Xu, Y. Liu, G. T. Hwang, S. J. L. Kang, Z. L. Wang and K. J. Lee, *Nano Lett.*, 2010, **10**(12), 4939–4943.
11 Y. Guo, K. Kakimoto and H. Ohsato, *Appl. Phys. Lett.*, 2004, **85**, 4121–4123.
12 Y. Wang, D. Damjanovic, N. Klein, E. Hollenstein and N. Setter, *J. Am. Ceram. Soc.*, 2007, **90**, 3485.
13 E. K. Akdoğan, K. Kerman, M. Abazari and A. Safari, *Appl. Phys. Lett.*, 2008, **92**(11), 112908.
14 B. Y. Zhang, J. G. Wu, X. J. Cheng, X. P. Wang, D. Q. Xiao, J. G. Zhu, X. J. Wang and X. J. Lou, *ACS Appl. Mater. Interfaces*, 2013, **5**(16), 7718–7725.
15 X. Wang, J. Wu, D. Xiao, J. Zhu, X. Cheng, T. Zheng, B. Zhang, X. Lou and X. Wang, *J. Am. Chem. Soc.*, 2014, **136**(7), 2905–2910.
16 K. Xu, J. Li, X. Lv, J. G. Wu, X. X. Zhang, D. Q. Xiao and J. G. Zhu, *Adv. Mater.*, 2016, **28**(38), 8519–8523.
17 T. Zheng, J. Wu, D. Xiao, J. Zhu, X. Wang, L. Xin and X. Lou, *ACS Appl. Mater. Interfaces*, 2015, **7**, 5927.
18 T. Zheng, J. Wu, D. Xiao, J. Zhu, X. Wang and X. Lou, *J. Mater. Chem. A*, 2015, **3**, 1868.
19 S. J. Zhang, R. Xia, T. R. Shrout, G. Z. Zang and J. F. Wang, *J. Appl. Phys.*, 2006, **100**, 104108.
20 S. J. Zhang, R. Xia and T. R. Shrout, *Appl. Phys. Lett.*, 2007, **91**, 132913.
21 F. Z. Yao, J. Glaum, K. Wang, W. Jo, J. Rödel and J. F. Li, *Appl. Phys. Lett.*, 2013, **103**, 19290.
22 L. Wu, D. Q. Xiao, J. G. Wu, Y. Sun, D. M. Li, J. G. Zhu, P. Yu, Y. Zhuang and Q. Wei, *J. Eur. Ceram. Soc.*, 2008, **28**, 2963–2968.
23 Y. Gao, J. L. Zhang, X. J. Zong, C. L. Wang and J. C. Li, *J. Appl. Phys.*, 2010, **107**, 074101.
24 K. Kakimoto, K. Akao, Y. Guo and H. Ohsato, *Jpn. J. Appl. Phys.*, 2005, **44**, 7064.
25 N. Klein, E. Hollenstein, D. Damjanovic, H. J. Trodahl, N. Setter and M. Kuball, *J. Appl. Phys.*, 2007, **102**, 014112.
26 M. H. Lee, D. J. Kim, J. S. Park, S. W. Kim, T. K. Song, M. H. Kim, W. J. Kim, D. Do and I. K. Jeong, *Adv. Mater.*, 2015, **27**, 6976–6982.
27 K. Wang, F. Z. Yao, W. Jo, D. Gobeljic, V. V. Shvartsman, D. C. Lupascu, J. F. Li and J. Rödel, *Adv. Funct. Mater.*, 2013, **23**, 4079–4086.
28 R. P. Wang, K. Wang, F. Z. Yao, J. F. Li, F. H. Schader, K. G. Webber, W. Jo and J. Rödel, *J. Am. Ceram. Soc.*, 2015, **98**, 2177–2182.
29 D. Xue, Y. M. Zhou, H. X. Bao, C. Zhou, J. H. Gao and X. B. Ren, *J. Appl. Phys.*, 2011, **109**, 054110.
30 E. L. Colla, S. Hong, D. V. Taylor, A. K. Tagantsev, N. Setter and K. No, *Appl. Phys. Lett.*, 1998, **72**, 2763.
31 N. M. Murari, S. Hong, H. N. Lee and R. S. Katiyar, *Appl. Phys. Lett.*, 2011, **99**, 052904.
32 D. Damjanovic, *J. Am. Ceram. Soc.*, 2005, **88**(10), 2663.
33 K. A. Schonau, L. A. Schmitt, M. Knapp, H. Fuess, R. A. Eichel, H. Kung and M. J. Hoffmann, *Phys. Rev. B: Condens. Matter Mater. Phys.*, 2007, **75**, 184117.
34 R. Theissmann, L. A. Schmitt, J. Kling, R. Schierholz, K. A. Schonau, H. Fuess, M. Knapp, H. Kungl and M. J. Hoffmann, *J. Appl. Phys.*, 2007, **102**, 024111.
35 S. Hong, B. Ecabart, E. L. Colla and N. Setter, *Appl. Phys. Lett.*, 2004, **84**, 2382.
36 M. Park, K. No and S. Hong, *AIP Adv.*, 2013, **3**, 042114.
37 G. A. Rossetti, A. G. Khachaturyan, G. Akcay and Y. Ni, *J. Appl. Phys.*, 2008, **103**, 114113.
38 H. J. Wu, D. Z. Xue, D. C. Lv, J. H. Gao, S. W. Guo, Y. M. Zhou, X. D. Ding, C. Zhou, S. Yang, Y. D. Yang and X. B. Ren, *J. Appl. Phys.*, 2012, **112**, 052004.

39 Y. Zhang, D. Z. Xue, H. J. Wu, X. D. Ding, T. Lookmanc and X. B. Ren, *Acta Mater.*, 2014, **71**, 176–184.
40 H. Wang, J. Zhu, X. W. Zhang, Y. X. Tang and H. S. Luo, *Appl. Phys. Lett.*, 2008, **92**, 132906.
41 J. H. Gao, Y. S. Hao, S. Ren, T. Kimoto, M. X. Fang, H. Y. Li, Y. Wang, L. S. Zhong, S. T. Li and X. B. Ren, *J. Appl. Phys.*, 2015, **117**, 084106.
42 J. H. Gao, D. Z. Xue, Y. Wang, D. Wang, L. X. Zhang, H. J. Wu, S. W. Guo, H. X. Bao, C. Zhou, W. F. Liu, S. Hou, G. Xiao and X. B. Ren, *Appl. Phys. Lett.*, 2011, **99**, 092901.
43 H. Wang, J. Zhu, N. Lu, A. A. Bokov, Z. G. Ye and X. W. Zhang, *Appl. Phys. Lett.*, 2006, **89**(4), 2908.
44 J. Fu, R. Z. Zuo, S. C. Wu, J. Z. Jiang, L. Li, T. Y. Yang, X. H. Wang and L. T. Li, *Appl. Phys. Lett.*, 2012, **100**, 122902.